



Unveiling the reaction pathway on Cu/CeO₂ catalyst for electrocatalytic CO₂ reduction to CH₄

Lei Xue^{a,1}, Chunjuan Zhang^{a,1}, Jinfang Wu^{a,*}, Qi-Yuan Fan^b, Yang Liu^a, Yanxin Wu^a, Jiaxin Li^a, Heng Zhang^a, Fenrong Liu^{a,*}, Shanghong Zeng^{a,*}

^a Inner Mongolia Key Laboratory of Chemistry and Physics of Rare Earth Materials, School of Chemistry and Chemical Engineering, Inner Mongolia University, Hohhot 010021, China

^b State Key Laboratory of Physical Chemistry of Solid Surface, College of Chemistry and Chemical Engineering, Xiamen University, Xiamen 361005, China

ARTICLE INFO

Keywords:

Cu/CeO₂
Intermediate
Reaction mechanism
DFT
CO₂ reduction

ABSTRACT

The determination of reaction mechanism for electrocatalytic CO₂ reduction by experiments is still out of reach on copper catalyst, which limits its advance towards industrial implementation. Here, the Cu/CeO₂ catalyst as paradigm was studied to validate the reaction intermediates and pathway. The Cu/CeO₂ catalysts with different morphologies were synthesized, and it is discovered that the nanorod Cu/CeO₂ catalyst exhibits high selectivity for CO₂-to-CH₄ with the highest turnover frequency for CH₄ production among the samples. Detailed study indicates that the nanorod Cu/CeO₂ possesses the largest electrochemically active surface area, higher proportion of O-vacancy sites, and better capability of CO₂ adsorption and activation. The chemical nature above together contributes to its high activity. Theoretical calculations reveal that the doping of Cu into CeO₂ can significantly lower the reaction energy barrier of *CO₂ → *COOH and change the reaction pathway from *CHOH → *CH₂OH to *CHOH → *CH, effectively improving the catalytic performance for CO₂ electroreduction.

1. Introduction

Electrocatalytic reduction of CO₂ (CO₂RR) to valuable fuels or chemical feedstocks via solar/wind generated electricity is a promising scalable strategy to address greenhouse CO₂ emission issues and realize a closed loop for carbon footprint [1–4]. In particular, the highly selective reduction of CO₂ to CH₄ or C₂H₄ has emerged as an attractive pathway because CH₄ and C₂H₄ can be widely used in civil and industrial production [5–8]. To realize selective CO₂ to CH₄ or C₂H₄, copper (Cu) has proven to be a possible choice of metal catalyst for accelerating sluggish CO₂RR involving multi-electron and proton transfer [9–15]. Nevertheless, the intrinsic challenge on Cu has been weak CO₂ adsorption, high overpotential, low efficiency and poor selectivity toward the target products in CO₂RR [16–19].

The intimate interfacial interaction has been suggested to be dominant in effectively improving molecular adsorption and activation [20–26]. Ceria (CeO₂) as a constituent or a catalyst support has gained considerable attention in heterogeneous catalysis due to its abundant O-vacancy sites, good oxygen storage capacity and excellent redox

properties originated from Ce³⁺/Ce⁴⁺ transition [27]. The unique features are favorable for the formation of metal-CeO_x nanointerface with highly active and selective catalytic sites, enabling the improved dispersion, molecular activation and catalytic performance [28,29]. In fact, catalytic performance of metal-doped CeO₂ is closely associated with defect structure on the interface, which can be tune via forming and eliminating O-vacancy sites at different CeO₂ surfaces [30]. For CeO₂, {111}, {110} and {100} are three thermodynamically most stable surfaces. The surface energy follows the order of {111} < {110} < {100}, while the formation energy of O-vacancy sites is in sequence of {110} < {100} < {111} [31]. A great effort was put on the precise control of surface atomic arrangements to modify the reactivity of metal-CeO_x nanointerface. For instance, Wang et al. reported that the cationic Ru species is formed on CeO₂ nanorods with the exposed {111} planes, resulting in the superior CO oxidation activity [28]. Liu et al. paid particular attention to CeO₂ crystal planes, and they found that the 2 Pd/CeO₂-R (rods) that exposes (110) facet exhibits the highest catalytic activity for CO₂ hydrogenation to CH₃OH among the as-studied catalysts with different crystal facets, attributing that abundant O-vacancy sites

* Corresponding authors.

E-mail addresses: jfwu@imu.edu.cn (J. Wu), fenrongli@163.com (F. Liu), zengshanghong@imu.edu.cn (S. Zeng).

¹ These authors contributed equally to this work and should be considered co-first authors

play a key role in CO₂ adsorption and activation [30].

Recently, CeO₂ has also successfully applied in CO₂RR for constructing effective metal-CeO_x nanointerface for CO₂ activation. For example, Bao et al. found that the Au-CeO_x and Ag-CeO_x catalysts display much higher activity and Faradaic efficiency (FE) relative to the pristine Au, Ag or CeO₂, confirming the interface-enhanced effect in CO₂RR [26]. The Mn-doped CeO₂ underwent two efficient elementary charge transfer reactions for electrocatalytic CO₂ to CO [32]. Interestingly, Cu/CeO₂ catalysts show near-optimal properties and fascinating activity in many heterogeneous reactions due to the presence of Cu²⁺/Cu⁺ and Ce⁴⁺/Ce³⁺ redox pairs, thereby they were also investigated for CO₂RR in several studies [29,33,34]. Typically, the single-atomic Cu substitution in {111} plane of CeO₂ leads to the formation of multiple O-vacancy sites, generating a highly active center around single Cu site and improving CO₂ reduction to CH₄ [33]. Buonsanti et al. corroborated that the Cu/CeO_{2-x} heterodimers exhibit high selectivity toward CO₂RR in contrast to hydrogen evolution reaction due to synergistic effect of the Cu-CeO_{2-x} interfaces [29]. Moreover, the CuO-CeO₂ interface interaction effectively stabilize Cu⁺ during CO₂ electroreduction to C₂H₄ [34]. Nevertheless, CO₂RR mechanistic reaction pathway on Cu/CeO₂ remains elusive notwithstanding some efforts have been made to identify the elementary steps and the rate-limiting step through in situ spectroscopies combined with theoretical calculations.

Herein, the Cu/CeO₂ catalyst as paradigm was studied for probing the reaction intermediates and overall reaction pathway during CO₂RR. To the best of our knowledge, direct acquisition of CO₂RR mechanism on Cu/CeO₂ catalyst is limited and challenging. The FE toward CH₄ can reach 49.3% with a turnover frequency of approximately 8000 h⁻¹ for the nanorod Cu/CeO₂ catalyst. Experimental and theoretical calculations indicate that the doping of Cu atom on CeO₂ surface lowers the reaction energy barrier of *CO₂ → *COOH and changes the reaction pathway from *CHOH → *CH₂OH to *CHOH → *CH, and Quasi in situ ATR-FTIR and in situ DRIFTS validate the presence of relevant intermediates in the reaction pathway.

2. Experimental and computational methods

2.1. Chemicals

Cerium (III) nitrate hexahydrate (Ce(NO₃)₃·6 H₂O, 99.5%) and sodium carbonate (Na₂CO₃, 99.5%) were purchased from Sinopharm Chemical Reagent Co., Ltd. Copper nitrate trihydrate (Cu(NO₃)₂·3 H₂O, ≥ 99%), polyvinyl pyrrolidone (PVP, (C₆H₉NO)_n, Mw = 44000) and sodium hydroxide (NaOH, ≥ 96%) were obtained from FengChuan Chemical Research Institute. Nafion solution (5.0 wt%) and Nafion membrane from Sigma-Aldrich were used as received.

2.2. Preparation of supports and catalysts

The CeO₂ supports with different morphologies were prepared based on methods adapted from the literature with some modifications [33,35,36]. The detailed procedures for the preparation of CeO₂ nanorods (CeO₂-R), nanocubes (CeO₂-C), nanoparticles (CeO₂-P) and nanospheres (CeO₂-S) were described in the Supporting Information.

Typical, 2.32 mmol of the as-synthesized CeO₂ support was added in 10 mL of deionized water containing 0.32 mmol of Cu(NO₃)₂·3 H₂O under stirring, followed by the addition of 2.38 mmol of Na₂CO₃. The resulting precipitate was collected by centrifugation, washed thoroughly with absolute ethanol, dried in a vacuum oven at 60 °C overnight, and calcined at 250 °C in 5% H₂/Ar mixture for 1 h at a heating rate of 5 °C min⁻¹. For simplicity, the as-synthesized catalysts were hereafter denoted as Cu/CeO₂-R, Cu/CeO₂-C, Cu/CeO₂-P and Cu/CeO₂-S according to their morphologies, respectively. The target nominal composition was 5 wt% Cu (the weight ratio of Cu to CeO₂).

2.3. Physicochemical characterizations

The structural information on the crystalline phase was derived from conventional X-ray diffraction (XRD) patterns, and the lattice parameter and average nanocrystalline sizes were analyzed using the High Score Plus software package. The Brunauer-Emmett-Teller (BET) specific surface area, pore volume and the pore structure of the catalysts were measured on a Micromeritics ASAP2020 adsorption apparatus, and the BET specific surface area was calculated from the data of N₂ physisorption isotherms. The structural disorder of the catalysts was determined by a Renishaw Micro-Raman spectrometer with an excitation laser of 532 nm. Morphology, elemental distribution and microstructures of the catalysts were characterized using transmission electron microscopy (TEM) and scanning electron microscopy (SEM) with an energy-dispersive spectroscopy (EDS) for elemental mapping. The composition was quantified by inductively coupled plasma optical emission spectrometry (ICP-OES) on an Agilent 5110 model. The elemental valence and composition of catalysts was measured using X-ray photoelectron spectroscopy (XPS) on a Thermo Fisher ESCALAB 250XI instrument. Auger LMM spectra were employed to identify the valence state of Cu species. The interaction between two species were investigated by Ultraviolet-visible (UV-vis) absorption spectra on a UV-visible system (U3900, Hitachi). The surface reaction information was studied by quasi in situ attenuated total reflection infrared spectroscopy (ATR-FTIR) on a Thermo Scientific Nicolet iS10 and in situ diffuse reflectance Fourier transform infrared spectroscopy (in situ DRIFTS) on a Thermo Scientific Nicolet iS50 FTIR spectrometer coupled with a MCT detector. The detailed characterizations were described in **Support Information**.

2.4. Electrocatalytic measurements

The electrocatalytic performance for CO₂RR was measured in an airtight H-type cell with an electrochemical workstation (CHI 760 E, Shanghai) at ambient temperature (see Supporting Information). The sample was prepared by dispersing 5.0 mg catalyst into 900 μL of ethanol and 100 μL of Nafion (Nafion 115, DuPont, USA), and the mixture was uniformly diffused on 1 × 1 cm² carbon paper. 0.1 M KHCO₃ saturated with CO₂ was filled with two compartments as electrolyte. The potentials given herein were not compensated for Ohmic loss (iR) and converted to the reversible hydrogen electrode (RHE) scale using the Eq. 1 (Nernst).

$$E(\text{vs. RHE}) = E(\text{vs. Ag/AgCl}) + 0.197 \text{ V} + 0.0591 \times \text{pH} \quad (1)$$

Prior to experiments, the cell was bubbled with CO₂ for 30 min under magnetically stirring to ensure CO₂ saturation in the electrolyte (see Supporting Information). The gaseous products from CO₂RR were online-detected by a gas chromatography (GC2014, Shimadzu) equipped with a thermal conductivity detector (TCD) for H₂ quantification and a flame ionization detector (FID) with methanizer for analysis of C₁ to C₃ hydrocarbons. Liquid products were determined by ¹H nuclear magnetic resonance spectroscopy (¹H NMR) on a Bruker Ascend 400 NMR spectrophotometer. Faradaic efficiency (FE) toward each product was calculated by the following Eq. 2.

$$\text{FE}\% = (n \cdot n_e \cdot F \times 100\%) / Q \quad (2)$$

where *n* is the mole number of electrons to participate in the Faradaic reaction, *n_e* is the number of exchanged electrons, *F* is the Faraday constant (96485 C mol⁻¹), and *Q* is the total charge.

Turnover frequency (TOF, h⁻¹) for CH₄ production was calculated using Eq. 3.

$$\text{TOF} = (I_{\text{CH}_4} / N) / (m_{\text{catalyst}} \times w / m_{\text{Cu}}) \times 3600 \quad (3)$$

where *I*_{CH₄} is the partial current of CH₄, *N* is the number of electrons transferred for products formation, *F* is the Faradaic constant (96485 C

mol^{-1}), m_{catalyst} represents catalyst mass in the electrode, w is mass percentage of Cu in the catalyst and m_{Cu} is atomic mass of Cu (63.5 g mol^{-1}).

2.5. Computational methods

Ab-initio calculations were conducted by spin-polarized density functional theory (DFT) as implemented in VASP software, coupled with the generalized gradient approximation (GGA) of the Perdew-Burke-Ernzerhof (PBE) for the exchange correlational functional. A plane wave basis set with a cut-off energy of 400 eV and projector augmented wave (PAW) were used to represent the valence electrons and core electrons, respectively. The convergence tolerance of the energy change and the maximum force were set to $1.0 \times 10^{-5} \text{ eV}$ and 0.01 eV/\AA , respectively. According to the HRTEM characterization, herein the 3D periodic slabs of CeO_2 (110) facet were chosen to interact with CO molecule. The slab model including three layers of 2×2 cell (6 Ce atoms and 12 O atoms) was adopted with a vacuum layer of 20 Å and Gamma k-point grid for surface calculations. The atoms in the bottom one atomic layer were fixed and the top two atomic layers were fully relaxed during geometry optimization. In order to simulate Cu/CeO₂ surface, one of Ce atom in the first layer of CeO_2 (110) model was replaced by a Cu atom, denoted as Cu/CeO₂ (110). The adsorption energy (E_{ad}) of gas molecules and intermediate products on model atomic configurations were calculated as follows:

$$E = E_{\text{adsorbate-slab}} - E_{\text{slab}} - E_{\text{adsorbate}} \quad (4)$$

where, $E_{\text{adsorbate-slab}}$, E_{slab} and $E_{\text{adsorbate}}$ are total energy for the slab with adsorbate complex, the isolated slab and the isolated adsorbate,

respectively. The Gibbs free energies (ΔG) of reaction steps were calculated using the formula described as follows:

$$\Delta G = \Delta E + \Delta \text{ZPE} - T\Delta S + \Delta G_{\text{pH}} + \Delta G_{\text{U}} \quad (5)$$

where ΔE is the total energy, ΔZPE is the difference corresponding to the zero-point energy, and $T\Delta S$ is the entropy contribution ($T = 298.15 \text{ K}$). The zero-point energies and entropies were obtained via computing the vibrational frequencies of surface species. ΔG_{pH} is the free energy correction of H^+ concentration, $\Delta G_{\text{pH}} = k_{\text{B}}T \ln 10 \times \text{pH}$, where k_{B} is the Boltzmann constant. ΔG_{U} is the effect of electrode potential (U), $\Delta G_{\text{U}} = -neU$, where n is the number of transferred electrons and U is applied electrode potential.

3. Results

3.1. Structural and morphological characterizations

Fig. S1 and Fig. 1a illustrate XRD patterns for the calcined supports and catalysts, respectively. The diffraction peaks match well with the face-centered cubic-fluorite CeO_2 structure (space group $Fm\bar{3}m$, PDF #081-0792). In stark contrast to the Cu/CeO₂-C and Cu/CeO₂-P samples with the clearly identified Cu (111) (PDF# 65-9026) at 43.3° (Fig. 1b), no recognizable diffraction peaks ascribed to Cu species appear in XRD patterns of the Cu/CeO₂-R and Cu/CeO₂-S, demonstrating that the Cu species is highly dispersed on the Cu-CeO₂ nanointerfaces (Fig. 1c) or it is incorporated into the CeO_2 matrix. Combined with the results of BET surface area in Table 1, it is inferred that the dispersion of Cu species is associated with the surface area.

Bragg formula and Scherrer equation were used to estimate lattice

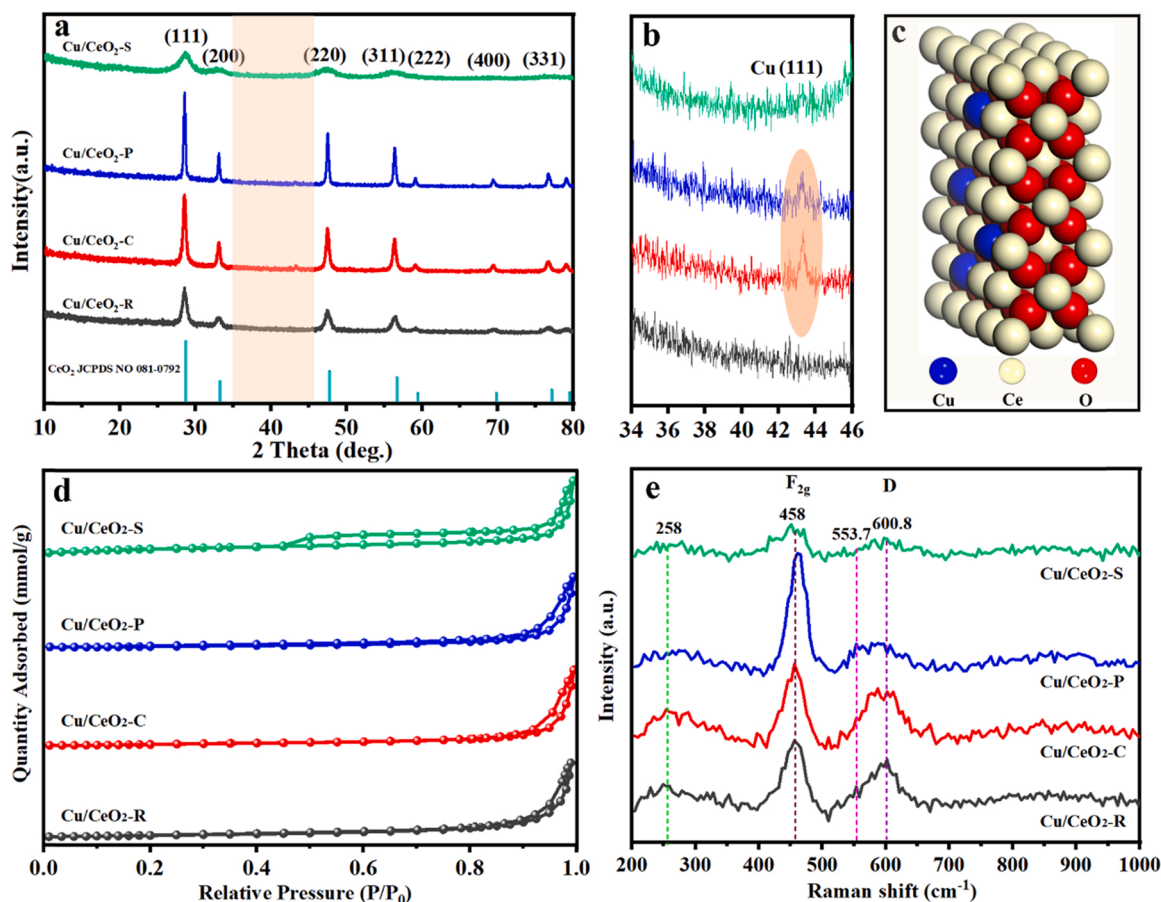


Fig. 1. (a) Representative XRD patterns of the Cu/CeO₂ catalysts. (b) The magnified Cu region. (c) Schematic illustration of the Cu/CeO₂ catalysts. (d) Nitrogen sorption isotherms. (e) Raman spectra of the Cu/CeO₂ catalysts.

Table 1
Physicochemical properties of the supports and catalysts.

Sample	CeO ₂ lattice parameter (Å) ^a	CeO ₂ Crystallite Size (nm) ^b	S _{BET} (m ² /g)	Pore Volume (cm ³ /g) ^c	Microstrain (Δd/d) ^d
CeO ₂ -R	5.414	13.52	112.4	0.50	0.01029
Cu/CeO ₂ -R	5.411	10.57	81.8	0.58	0.01314
CeO ₂ -C	5.411	23.26	38.6	0.23	0.00597
Cu/CeO ₂ -C	5.413	23.37	29.8	0.25	0.00594
CeO ₂ -P	5.410	21.40	40.8	0.32	0.00648
Cu/CeO ₂ -P	5.412	24.20	31.6	0.36	0.00571
CeO ₂ -S	5.421	7.21	103.2	0.26	0.01930
Cu/CeO ₂ -S	5.415	7.25	50.3	0.19	0.01915

^a Calculated from XRD measurements via Bragg's formula.

^b Calculated from the Scherrer equation.

^c Calculated from the desorption branch of the isotherm using BJH model.

^d Based on analysis of the XRD peaks via Williamson-Hall linear fittings.

parameters and average crystallite sizes (Table 1), respectively. By contrast, the lattice parameters of Cu/CeO₂-R and Cu/CeO₂-S are smaller relative to those of their corresponding supports, implying that Cu species might be inserted into CeO₂ unit cell, which results in the lattice distortion because of the significant lattice mismatch between Cu and CeO₂. The average crystallite sizes of CeO₂ decrease in the order of Cu/CeO₂-P, Cu/CeO₂-C, Cu/CeO₂-R and Cu/CeO₂-S, which is consistent with the crystallinity of the catalysts. In the cases of Cu/CeO₂-R and Cu/CeO₂-S, the broadening peaks of the CeO₂ are indicative of their poorly crystalline nature. Accordingly, the catalysts with nanorod and nanosphere morphologies exhibit relatively higher surface area than the nanocube and nanoparticle samples. Intriguingly, they also possess a larger microstrain in contrast with the other two counterparts (Table 1), suggesting that an enhanced distortion is obtained for the catalysts with nanorod and nanosphere morphologies. Specifically, an increase of microstrain is induced upon Cu incorporation to CeO₂ lattice for the rod-like catalyst.

Textural properties were determined by recording N₂ adsorption-desorption isotherms. The CeO₂-R and CeO₂-S before Cu doping possess higher surface area than the CeO₂-P and CeO₂-C (Table 1), thus resulting in higher dispersion of Cu species, which is in agreement with the XRD analyses in Fig. 1b. Type IV isotherms (Fig. 1d) with a H2 hysteresis loop for nanospheres and H1 hysteresis loops for nanorods, nanocubes and nanoparticles signify the presence of mesopores in the catalysts. Specific surface areas of the as-prepared Cu/CeO₂ catalysts (Table 1) based on the Brunauer-Emmett-Teller (BET) theory vary from 31 to 82 m² g⁻¹, suggesting that the support morphology has a certain effect on the surface area. BET areas follow the order of Cu/CeO₂-R > Cu/CeO₂-S > Cu/CeO₂-P > Cu/CeO₂-C. In more detail, the Cu/CeO₂-R possesses the largest surface area and pore volume in the four samples, attractive for an efficient exposure of the active sites. Also, the pores centered at about 2 nm (Fig. S2) are from both the accumulation of nanocrystals and the holes inside nanorods derived from the defects.

Considering the crucial role of defects in activating CO₂ molecule, the defect structure in the catalysts was examined by Raman scattering (Fig. 1e). The weak peaks at ~258 cm⁻¹ are assigned to a second-order transverse acoustic mode (2TA). The strong peaks positioned at approximately 458 cm⁻¹ correspond to the F_{2g} symmetric breathing mode of O atoms in the cubic-fluorite CeO₂ structure (Ce-O-Ce vibration), and its location and shape can be regulated with the change of crystallite size [37]. In contrast, the Raman peak of F_{2g} mode in the spectrum of nanosphere catalyst is weaker relative to those of the other

samples due to the smallest crystallite size. The overlapping peaks from 520 to 650 cm⁻¹ are attributed to the defect induced mode (D), which is correlated with the deformation of the anionic lattice [38]. The D band is comprised of two components. Specifically, the relatively weak peak at 553.7 cm⁻¹ is ascribed to O-vacancy sites, and the stronger peak at 600.8 cm⁻¹ is assigned to the lattice distortions in the CeO₂ lattice [39]. The quantitative measurement of concentration of defect sites in the catalysts can be calculated via the relative intensity of D and F_{2g} (denoted as I_D/I_{F2g}). The I_D/I_{F2g} ratio that is commensurate to the structural defects follows the order of Cu/CeO₂-R > Cu/CeO₂-S > Cu/CeO₂-C > Cu/CeO₂-P (Table 2). Taken together, the XRD pattern and Raman spectrum confirm the existence of abundant defects in the Cu/CeO₂-R sample.

The morphology, size-uniformity and composition distribution of the as-prepared catalysts were confirmed by SEM and TEM characterizations (Fig. S3 and Fig. 2). The catalysts are assembled from small nanocrystals (<25 nm, Table 1) into the relatively uniform morphologies. The morphologies of supports are essentially preserved upon Cu doping. EDS mapping of the rod-like sample verifies a uniform dispersion of Ce and O elements, whilst Cu has a sparser distribution (Fig. S3a1-a4). The nanorods are 8~15 nm in diameter and 200~300 nm in length with a growth direction along CeO₂ (110) facet, displaying a stacked and staggered distribution with abundant pores about 2 nm inside the nanorods (Fig. 2a). These pores might provide the channels for the transmission of CO₂, electrolyte, intermediates and products into and out of the catalyst layer. The lattice spacings of the two domains assignable to CeO₂ (110) crystallographic orientation can be identified from the HRTEM image, and it suggests that (110) is preferentially exposed facet in the case of nanorods. The dislocation and lattice distortion are observed in high-resolution TEM image, manifesting that the structural defects near the tips are formed for alleviating the tensile strain in the nanorod catalyst, in line with the results of XRD and Raman. Taking a closer look at the tips and edges, the edges of nanorods are curved, which offer abundant stepped and low-coordinated sites for stabilizing Cu species at the nanointerface [39]. That is, the large BET surface area and high density of surface defects not only improve the dispersion of catalytically active species, but also might anchor Cu species to restrain its growth, in good accordance with the XRD and EDS analyses.

The nanocubes with size ranging from 10 to 50 nm are enclosed by well-defined CeO₂ (100) facets, as evidenced by the lattice spacing of 0.27 nm found in Fig. 2b. Evidently, the nanocubes have smooth surfaces, and the round-shaped and curved corners are observable. The nanoparticles with a diameter of around 50~70 nm preferentially expose CeO₂ (111) crystal plane (Fig. 2c). The smooth surface and the observed high crystallinity of the nanocube and nanoparticle catalysts are agreement with the results from XRD. The nanosphere is a single-shelled hollow structure with a diameter of about 200 nm (Fig. 2d). The surface is rough, which is beneficial to the distribution of active components. From the corresponding fast Fourier transform (FFT, inset) and HRTEM image, the predominately exposed facets are CeO₂ (311) surface with some (110) and (111) planes at the edges. The atomic arrangements are different in nature on basal CeO₂ (111), (110) and (100) facets, resulting in the different geometrical and electronic properties of surface cerium. The electron density follows the order of (100) > (110) > (111). However, this order is reversed to the Lewis acidity [40].

3.2. Elemental composition and surface chemistry

The composition of the two elements were quantified by ICP-OES, and the obtained weight ratios are in good accordance with the Cu/CeO₂ theoretical values (Table 2). The valence states and surface chemistry of the as-synthesized samples were elucidated by XPS characterization. The peaks of Cu 2p, Ce 3d, O 1s and C 1s are clearly identified in the wide-angle survey spectra (Fig. S4). It is noted that the Cu 2p core-level spectra are comprised of the Cu 2p_{3/2} and Cu 2p_{1/2}

Table 2

Composition, surface properties and band gap of the catalysts.

Catalyst	Cu wt% ^a	I _D /I _{R2g} ^b	Cu ⁰ %	Cu ⁺ %	Cu ²⁺ %	Ce ³⁺ % ^c	O _{ad} / (O _{ad} + O _L) ^c	Cu/Ce	Band gap (eV) ^d
Cu/CeO ₂ -R	4.91	0.67	12.1	45.3	42.6	22.1	0.42	0.13	2.31
Cu/CeO ₂ -C	4.65	0.58	7.3	59.2	33.5	19.9	0.36	0.19	2.73
Cu/CeO ₂ -P	4.77	0.18	16.0	51.5	32.5	13.4	0.30	0.17	2.95
Cu/CeO ₂ -S	4.87	0.66	33.6	39.5	26.9	24.9	0.46	0.15	2.62

^a Measured by ICP-OES (weight ratio of Cu to CeO₂); ^b Calculated from Raman spectra; ^c Calculated from XPS analyses of catalyst surface; ^d Calculated from UV–vis Spectra.

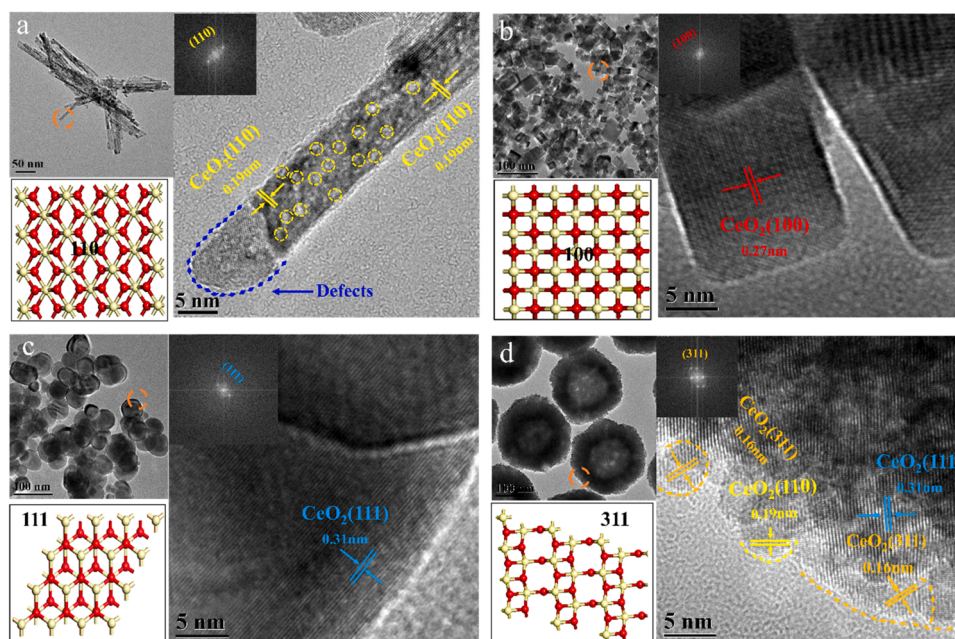


Fig. 2. TEM and HRTEM images of the Cu/CeO₂ catalysts with different morphologies: (a) nanorods, (b) nanocubes, (c) nanoparticles, and (d) nanospheres. (Inset: perspective view of (110), (100), (111) and (311) facets of cubic-fluorite CeO₂).

peaks. Specifically, the XPS spectra of Cu 2p_{3/2} were fitted into two peaks at 933.8 eV and 932.5 eV (Fig. 3a), corresponding to CuO and the reduced Cu species (Cu⁰/Cu₂O), respectively. The oscillating satellite peaks are typical characteristics of the presence of CuO. It indicates the existence of partially oxidized Cu species. Based on cumulative fitting and calculation from XPS and Auger LMM spectra (Fig. 3b), three valence states of Cu species can be quantitatively distinguished on the catalyst surface (Table 2). Herein, most of the Cu on the surface is oxidized to monovalent and divalent Cu species. The copper oxide species originate from the inevitable oxidation of Cu surface when exposure in the ambient air. The Cu/CeO₂-R sample possesses the most surface divalent Cu species due to highly dispersed and sparse distribution of Cu species on the nanorods, in accordance with the EDS mapping. It is proposed that there is an intimate correlation between the chemical state of Cu and the product selectivity for CO₂RR [14,15]. The metallic Cu is not the only state under realistic reaction conditions [41].

The XPS spectra of Ce 3d are complicated due to the hybridization of Ce 3d and O 2p orbitals as well as partial occupation of the Ce 4f orbitals, which can be deconvoluted into two spin-orbit doublets, and denoted as U and V in Fig. 3c, respectively. The six peaks located at 882.8 eV (V), 889.2 eV (V'), 898.5 eV (V''), 901.2 eV (U), 907.9 eV (U') and 916.9 eV (U'') are assigned to Ce⁴⁺, and the four peaks positioned at 881.4 eV (V'), 884.9 eV (V), 899.6 eV (U') and 903.1 eV (U) are ascribed to Ce³⁺, suggesting that Ce⁴⁺ and Ce³⁺ coexist in the hybrid system. The percentage of Ce³⁺ calculated from the area ratio of the sum of Ce³⁺ to that of total cerium species is higher on the surface of nanorod and nanosphere catalysts relative to the other two samples (Table 2). The density of O-vacancy sites is directly related to the Ce³⁺

concentration because O-vacancy sites must be accompanied by Ce³⁺ to keep electroneutrality in the *Fm* $\bar{3}$ *m* structure [29]. Whereby, the proportion of O-vacancy sites is in the sequence of Cu/CeO₂-S > Cu/CeO₂-R > Cu/CeO₂-C > Cu/CeO₂-P.

Furthermore, the XPS peaks of O 1s are deconvoluted into two peaks (Fig. 3d), which are assigned to lattice oxygen (O_L) at 529.7 eV and adsorbed oxygen (O_{ad}) on oxygen deficiency regions at 531.3 eV, respectively [42,43]. The proportion of O_{ad} derived from O_{ad} / (O_{ad} + O_L) follows the order of Cu/CeO₂-S (0.46) > Cu/CeO₂-R (0.42) > Cu/CeO₂-C (0.36) > Cu/CeO₂-P (0.30), signifying that there are more non-stoichiometric oxygen deficient sites on the surface of Cu/CeO₂-S (0.46) and Cu/CeO₂-R samples relative to the other two counterparts, in accordance with the above analysis on the proportion of O-vacancy sites. In stark contrast to the other three catalysts with the higher surface Cu/Ce atomic ratios from XPS than the nominal composition (molar ratio=0.13), the surface Cu/Ce ratio of the Cu/CeO₂-R sample is same as the nominal one (Table 2), demonstrating that the rich porous architecture of the rod-shaped sample facilitates the dispersion of active Cu species within the catalyst, attractive for a favorable contact between the CO₂RR-relevant species and active sites.

The surface coordination and oxidation state of Cu and Ce were further examined by UV–vis absorption spectra. In more detail, the absorption peaks located at 258 nm correspond to O²⁻ to Ce³⁺ charge transfer transitions (Fig. 4a), whilst the peaks positioned at 295 nm and 340 nm are ascribed to O²⁻ to Ce⁴⁺ charge transfer and interband transitions, respectively [44]. Herein, the as-prepared samples have the obvious Ce³⁺ and Ce⁴⁺ absorption peaks, signifying the coexistence of Ce³⁺ and Ce⁴⁺ in the nanostructures, in accordance with XPS analyses.

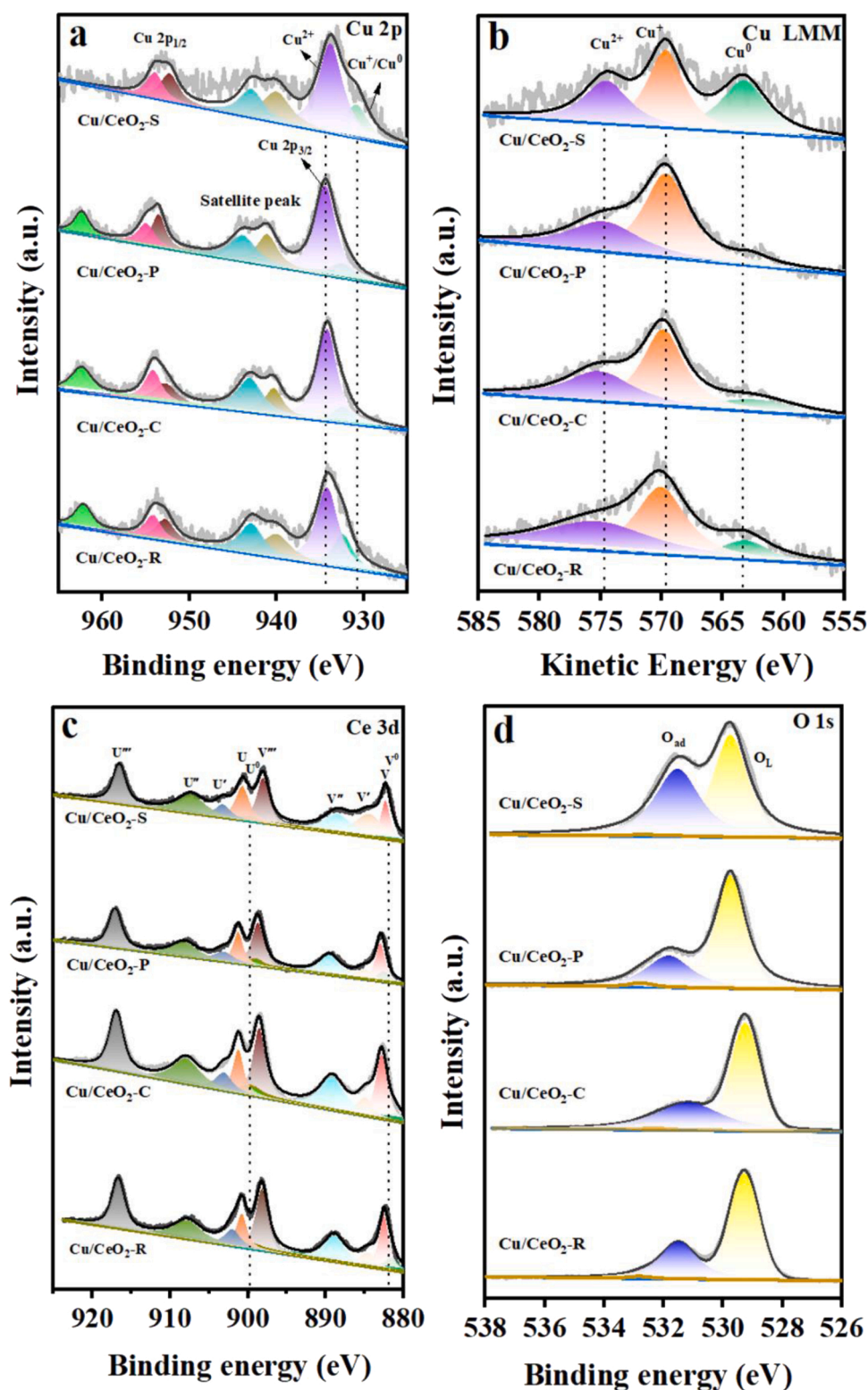


Fig. 3. High-resolution XPS spectra of the Cu/CeO₂ catalysts with different morphologies. (a) Cu 2p, (b) Cu LMM Auger spectra, (c) Ce 3d and (d) O 1s.

The Cu introduction triggers a blue shift of absorption profile at 340 nm, which proves that the Cu species might be inserted into the CeO₂ unit cell.

Furthermore, the peaks located at 280 nm and 750 nm belong to Cu²⁺ (Fig. 4b), and the broad peaks at 600 nm indicate the presence of Cu⁰ [45]. By contrast, the Cu/CeO₂-S shows the strong absorption peak of Cu⁰, while the Cu/CeO₂-R displays the strong profile of Cu²⁺, in line

with the XPS results, suggesting that the rod-shaped structure is beneficial to the Cu²⁺ formation at the nanointerfaces. As aforementioned, the Cu/CeO₂-S and Cu/CeO₂-R catalysts possess more O-vacancy sites. It is proposed that the O-vacancy sites might improve the reducing capability of copper catalyst, in favor of the valence transformation of copper species and the mobility of oxygen at the nanointerfaces during catalysis [46]. The band gap of the catalysts was calculated from the results of

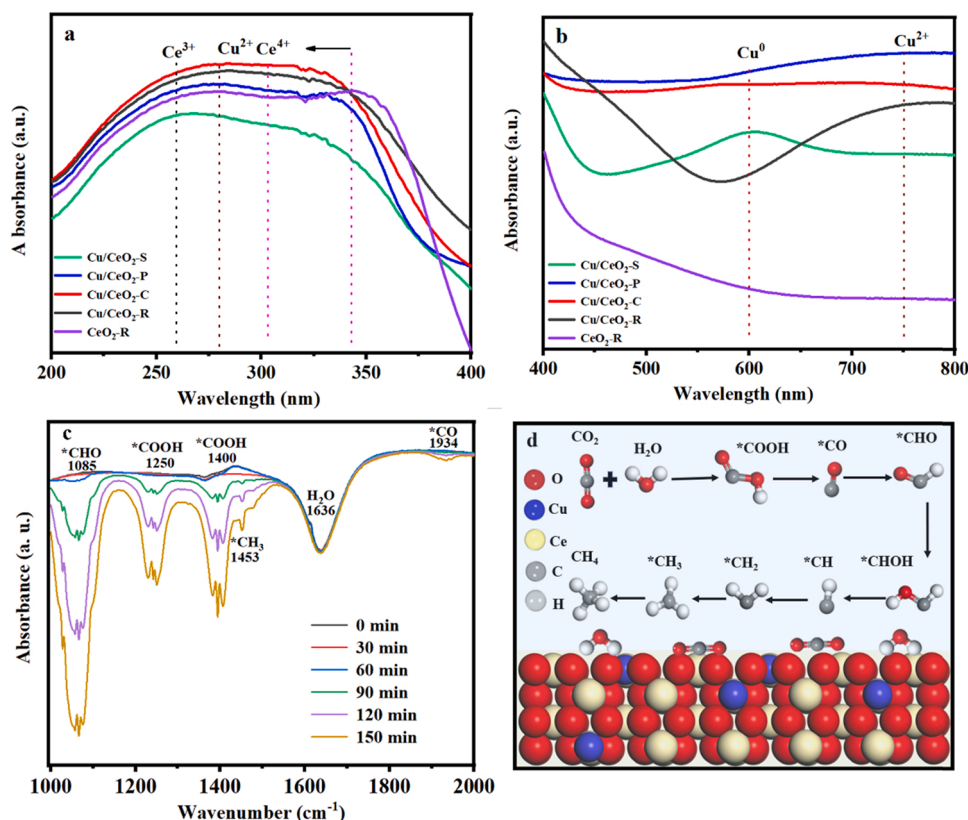


Fig. 4. (a, b) UV-vis spectra of the Cu/CeO₂ catalysts with different morphologies. (c) Quasi in situ ATR-FTIR spectra of the Cu/CeO₂-R in CO₂-saturated 0.1 M KHCO₃ aqueous solution at -1.6 V vs. RHE over time. (d) Schematic illustration of the reaction process including the reaction intermediates on the Cu/CeO₂-R catalyst.

UV-vis spectra (Fig. S5). Notably, the Cu doping decreases the band gap energies of the Cu/CeO₂-R, Cu/CeO₂-C and Cu/CeO₂-S (Table 2) in comparison with those of the corresponding CeO₂ (CeO₂-R: 2.86 eV; CeO₂-C: 2.76 eV; CeO₂-S: 2.70 eV) in Fig. S5, while the band gap energy increase for the Cu/CeO₂-P sample after Cu doping. Therein, the decrease of band gap is in the sequence of Cu/CeO₂-C, Cu/CeO₂-S and Cu/CeO₂-R, demonstrating that the interaction between Cu and CeO₂ follows the order of Cu/CeO₂-R > Cu/CeO₂-S > Cu/CeO₂-C > Cu/CeO₂-P. The interaction between two constituents is favorable for the generation of synergistic effect and the enhancement of catalytic activity [47].

The formation and transformation of the reaction intermediates during CO₂RR were investigated by quasi in situ ATR-FTIR. Fig. 4c shows FTIR spectra of the Cu/CeO₂-R in CO₂-saturated electrolyte at -1.6 V vs. RHE over time. The peaks at 1085 cm⁻¹ are ascribed to the characteristic band of *CHO that is the intermediate from CO₂ to CH₄ in CO₂ photoreduction [48], whilst the two bands located at 1250 cm⁻¹ and 1400 cm⁻¹ correspond to the stretching mode of *COOH [49]. Also, the peaks at 1453 cm⁻¹ are related to the C-H bending mode of *CH₃, the O-H bending mode of water is positioned at around 1636 cm⁻¹ [50], and a weak and asymmetric band located at 1934 cm⁻¹ corresponds to the dissolved CO in the solution. The peaks of *CHO, *COOH, *CH₃ and *CO gradually increase in intensity over time, especially for *CHO and *COOH, which are the indispensable intermediates for CO₂RR to CH₄ during catalysis. Coupled with DFT calculations, Fig. 4d gives an illustration of reaction process including the reaction intermediates on the Cu/CeO₂-R catalyst.

The adsorption behavior of CO₂ and surface-adsorbed molecules relevant to CO₂RR were investigated on the surface of Cu/CeO₂-R and Cu/CeO₂-S catalysts via in situ DRIFTS (Fig. 5 and Fig. S6). The absorption bands at about 1080 cm⁻¹ and 1395 cm⁻¹ are related to CO₃²⁻ stretch vibration, while the bands at near 1218 cm⁻¹ and 1640 cm⁻¹ are

assigned to HCO₃⁻ or related species that are chemisorbed on the CeO₂. The peak at about 1682 cm⁻¹ corresponds to the CO₂ *⁻ species, signifying that CO₂ molecule chemisorbed on the surface CeO₂ acquires an electron to involve in the activation of CO₂ [20,51]. It is proposed that C-O stretching modes of CO species adsorbed on Cu⁰, Cu⁺ and Cu²⁺ appear at about 2000–2100 cm⁻¹, 2115 cm⁻¹ and 2170 cm⁻¹, respectively [52,53]. Herein, the bands of CO adsorption on Cu⁰, Cu⁺ and Cu²⁺ species cannot be observed, and the possible reason is that the adsorbed CO* species are rapidly protonated into *CHO. This is evidenced by the above FTIR results, wherein the peaks of CO* are far lower than those of the corresponding *CHO species. The peak at about 2350 cm⁻¹ is ascribed to the stretching mode of CO₂ molecules. In addition, the multiple peaks in the range of 3600–3750 cm⁻¹ are attributed to the surface hydroxyl from the dissociation of H₂O molecules [20,54]. And the bands at about 3650 and 3710 cm⁻¹ correspond to Ce³⁺-OH and Ce⁴⁺-OH, respectively.

The adsorption strength of carbonaceous species directly affects the efficiency of catalytic CO₂ reaction [55]. The evolution of various bands as a function of time was investigated on the Cu/CeO₂-R and Cu/CeO₂-S catalysts. In the first 2 min, CO₂ adsorption is visible in the spectra with the formation of surface CO₃²⁻, HCO₃⁻, CO₂ *⁻ and hydroxyl species. When the time increases from 2 to 180 min, the intensity of all the carbonate bands increases for the two catalysts, manifesting that these species are gradually accumulated on the surface of catalysts over time. Afterwards the strength of the absorption bands remains almost unchanged in 120 min, indicative of the adsorption equilibrium on the catalyst surface. In contrast, the band intensities of CO₂ and CO₂ *⁻ on the Cu/CeO₂-R are stronger than those on the Cu/CeO₂-S, demonstrating that the Cu/CeO₂-R has better capability of CO₂ adsorption and activation, and consequently in favor of CO₂RR. The additional information was provided in the hydroxyl region (Fig. 5 and Fig. S6). The stronger bands of the mono-coordinated hydroxyls (Ce⁴⁺-OH) and doubly

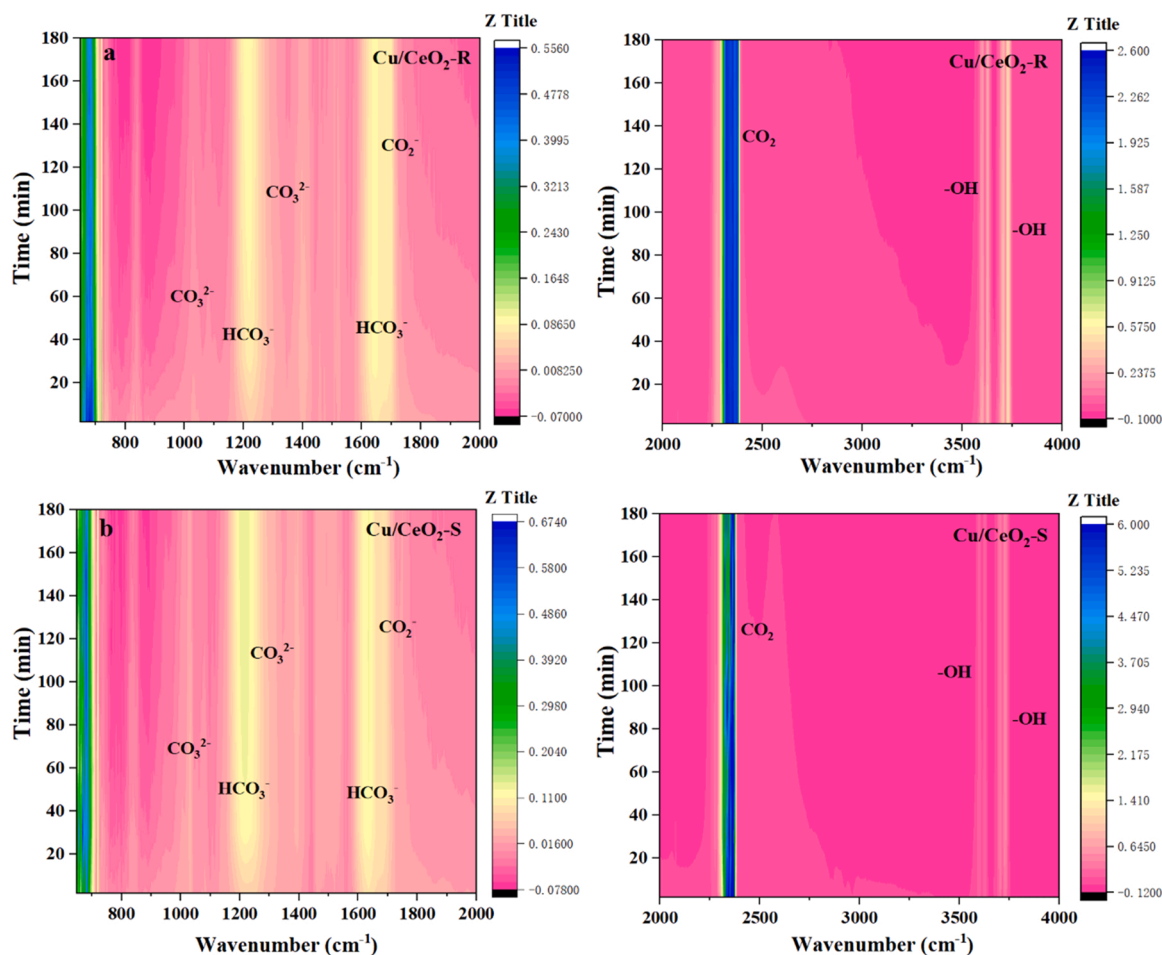


Fig. 5. *In situ* DRIFTS of the Cu/CeO₂-R (a) and Cu/CeO₂-S (b) catalysts under a humid CO₂ stream as a function of time.

bridging hydroxyls (Ce³⁺-OH) in the spectra of Cu/CeO₂-R are observed relative to those in the Cu/CeO₂-S, indicating that the surface of Cu/CeO₂-R sample is more favorable for the dissociation of H₂O into hydroxyls. The discrepancy substantiates that the catalyst morphology has an influence on the adsorption of CO₂ and surface-adsorbed molecules relevant to CO₂RR during reduction.

3.3. Electrocatalytic properties for CO₂RR and stability

The CO₂RR performance of the as-synthesized catalysts was evaluated in N₂ and CO₂-saturated 0.1 M KHCO₃ electrolyte. The current density in CO₂-saturated electrolyte is much higher than that in N₂-purged solution (Fig. S7), signifying a CO₂RR activity. By contrast, the Cu/CeO₂-R has the highest current density relative to the counterparts in the applied potentials (Fig. 6a). In more detail, the main products are C₂H₄, CO and H₂ on the pristine Cu (Fig. S8), and Faradaic efficiency for H₂ production is attributed to hydrogen evolution reaction (HER). Intriguingly, the Cu/CeO₂ catalysts exhibit a clear CH₄ selectivity in addition to C₂H₄, CO and H₂ (Fig. 6b-e). The Cu/CeO₂-R catalyst exhibits the highest current density among the samples, and the current density reaches maximum with a 49.3% Faradaic efficiency of CH₄ at -1.6 V. At this potential, a small quantity of liquid products was detected by ¹H NMR, as shown in Fig. S9. The intrinsic activities of the catalysts were estimated using CH₄ turnover frequency (TOF, Fig. S10) [56]. Notably, the Cu/CeO₂-R sample exhibits the highest TOF value for CH₄ production among the catalysts, which is about 2.2 times that of Cu/CeO₂-C, and 2.7 times that of Cu/CeO₂-P and 3.0 times that of Cu/CeO₂-S.

The electrochemically active surface area (ECSA), reflecting

catalytically active sites, is approximately proportional to the double-layer capacitance (C_{dl}), which was estimated using the C_{dl} by collecting CV curves at different scan rates (Fig. S11). The obtained ECSA follows the order of Cu/CeO₂-R > Cu/CeO₂-S > Cu/CeO₂-P > Cu/CeO₂-C (Table S1), in accordance with the BET results, revealing that the Cu/CeO₂-R catalyst, with an increase in surface roughness due to the presence of pores, defects and deep ledges, can afford more electrochemically accessible active sites to contact the electrolyte for adsorption and reduction of CO₂ in the catalytic reaction. The Cu/CeO₂-R catalyst shows the highest activity and specific activity both before and after normalized by the ECSA (Table S1). Tafel plots were recorded aiming to obtain an in-depth understanding on the kinetic mechanism of CO₂RR. The Tafel slopes for all samples in Fig. 6f are much higher than 118 mV dec⁻¹, implying that the rate-determining kinetics of CO₂RR on all catalyst surfaces depends greatly on the diffusion-controlled mechanism outside electron transfer process. Furthermore, the Tafel slope for Cu/CeO₂-R sample is estimated to be 335 mV dec⁻¹, which is minimum among the samples. The lowest Tafel slope for Cu/CeO₂-R is favorable for provoking the electrocatalytic activity due to the fastest electron transfer from the electrode to catalyst. That is, the first electron-transfer to the adsorbed CO₂ molecule facilitates to form *CO₂, which is protonated to boost a second electron-transfer to generate *COOH. In addition, the kinetics of electron transfer was examined using electrochemical impedance spectroscopy (EIS). The Cu/CeO₂-R sample exhibits the smallest charge transfer resistance than the other counterparts (Fig. 6g), demonstrating its faster charge transfer from the catalyst surface to the adsorbed CO₂ molecule in the electrolyte to form *CO₂ intermediate [57]. Furthermore, the adsorption of OH⁻ as a substitute for *CO₂ was conducted by single oxidative LSV scans over the catalysts in a

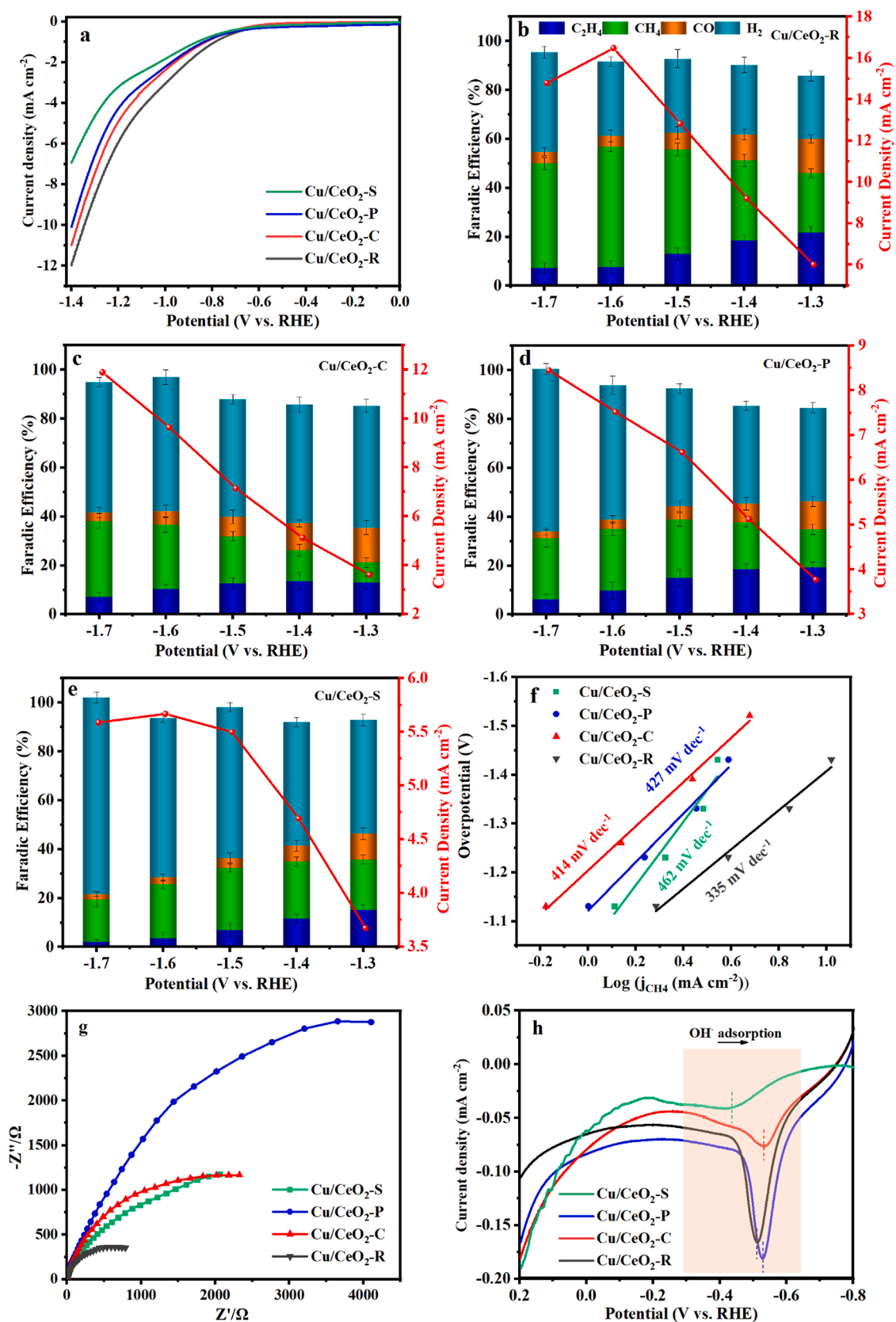


Fig. 6. (a) Linear sweep voltammetry (LSV) curves in CO₂-saturated 0.1 M KHCO₃ aqueous solution at room temperature. (b-e) Faradic efficiencies for C₂H₄, CH₄, CO and H₂ on the catalysts and current density. (f) Tafel plots of the catalysts toward CH₄ production. (g) Nyquist plots. (h) Single oxidative LSV scans at 50 mV s⁻¹ in N₂-saturated 0.1 M NaOH.

N₂-saturated 0.1 M NaOH electrolyte, aiming to probe the binding strength of the *CO₂ reactant intermediate on the catalyst surface. The potential is more negative on the Cu/CeO₂-P and more positive on the Cu/CeO₂-S for oxidative adsorption of OH⁻, signifying the stronger and weaker binding strength for OH⁻ adsorption, respectively (Fig. 6h). The Cu/CeO₂-R catalyst exhibits a moderate potential and a higher adsorption capacity in comparison with the other samples, implying a medium-strength binding of *CO₂ on this catalyst, which is in favor of stabilizing and activating the *CO₂ reactant intermediate for the overall CO₂ reduction, in accordance with the superior activity of the Cu/CeO₂-R catalyst for CO₂RR.

The stability is of great importance for the practical applications of CO₂RR electrocatalyst, and it is pointed out that the chemical state of Cu ions can reach well-stabilized state about 5 min toward zero-valent Cu in the electrochemical reaction [58]. The experimental test was accomplished on the Cu/CeO₂-R sample by performing electrocatalysis at -1.6 V vs. RHE for 3.5 h (Fig. S12). The Cu/CeO₂-R catalyst displays a relatively stable FE of CH₄ in 210 min, followed by a slight decline FE of C₂H₄ and an obvious increase in FE of H₂, which could be originated from the slight modulation of chemical state of Cu during electrocatalysis. Post-CO₂RR SEM image of the Cu/CeO₂-R catalyst indicates that the rod-shaped morphology is preserved in spite of the appearance of block particles at the surface (Fig. 7a). TEM images corroborate the maintenance of rod-like structure during the electrochemical reaction (Fig. 7b and c). Therein, lattice spacing of the CeO₂ with preferential orientation along the (110) direction is observable, and the formation energy of O-vacancy sites follows the order of {110} < {100} < {111} [31]. Lattice spacing of Cu is hard to find except for the location shown in Fig. 7c, suggesting that the Cu species is still highly dispersed on the Cu-CeO₂ nanointerfaces, which is related to the existence of O-vacancy sites on CeO₂ (110) facets in the Cu/CeO₂-R sample. Sasahara et al. pointed out that the adatoms in the O-vacancy sites are not mobile [59]. Parkinson et al. showed that single Au adatoms exclusively adsorb the narrow hollow sites [60]. The abundant pores were observed in post-CO₂RR TEM and HRTEM images of the Cu/CeO₂-R catalyst (Fig. 7b and c). The structural defects still appear near the tips of the nanorod catalyst in high-resolution TEM image. Moreover, the peak corresponding to Cu species is unrecognizable in the post-CO₂RR XRD patterns and Raman spectra, confirming good dispersion of Cu species on the nanorods during CO₂RR (Fig. S13 and S14). In contrast, the characteristic peaks of CeO₂ and carbon are confirmed. That is, high density of the

surface defects not only improve the dispersion of catalytically active species, but also might anchor Cu species to restrain its aggregation.

Fig. S14 compares Raman spectra of the fresh and post-electrocatalysis Cu/CeO₂-R at different potentials. Notably, the F_{2g} signals at 458 cm⁻¹ weaken as the potential increases, suggesting that the CeO₂ on the catalyst surface is gradually reduced in the CO₂RR, especially at high potentials. Operando XPS coupled with *ex situ* characterizations validate the partial reduction of CeO₂ during electrocatalysis [29]. Chen's group reported that the stable oxidation of Cu during electrocatalysis is crucial because it determines the distribution of products, rather than the others parameters, including morphology, atomic arrangement and structure, and so on [58,61]. The reoxidized behavior is revealed by the in situ XPS and in situ Raman. The spontaneous redox shuttle of Cu species ensures the steady chemical composition on the surface although the surface state of electrocatalysts is dynamic during CO₂RR, evidenced by quantitative XANES and EXAFS analyses [14,41,61]. In this work, the partial reduction of CeO₂ renders the presence of O-vacancy sites on CeO₂ (110) facets, stabilizing Cu atoms on vacancy sites. Furthermore, the abundant O-vacancy sites are paramount in CO₂ adsorption and activation [30].

3.4. DFT theoretical calculations

DFT calculations were carried out to understand the details of mechanism involved in the adsorption and activation of CO₂ molecules on the surface of pristine CeO₂ and Cu/CeO₂ catalysts. As shown in Fig. 8a, the adsorbed CO₂ molecule could undergo the first hydrogenation step to stable *COOH intermediate. Clearly, the free energy barrier of *COOH formation is negative on Cu/CeO₂, suggesting that the hydrogenation of *CO₂ → *COOH is exothermic and thermodynamically feasible on Cu/CeO₂ catalyst. Instead, the reaction is difficult on pristine CeO₂ catalyst, indicating the addition of Cu facilitates the hydrogenation reduction of *CO₂.

Specifically, as seen in Fig. 8b and Table S2, the introduction of Cu atom could regulate the adsorption configuration of CO₂ molecule, thereby causing the moderate adsorption energy of CO₂ on Cu/CeO₂. Therefore, it is proposed that the Ce species offers adsorption sites for CO₂ molecular, while the Cu species optimize the adsorption configuration of CO₂ by lowering its adsorption energy, allowing for the optimized C-O breaking and the enhancement of activity and selectivity toward CH₄ production. A second hydrogenation step takes place from

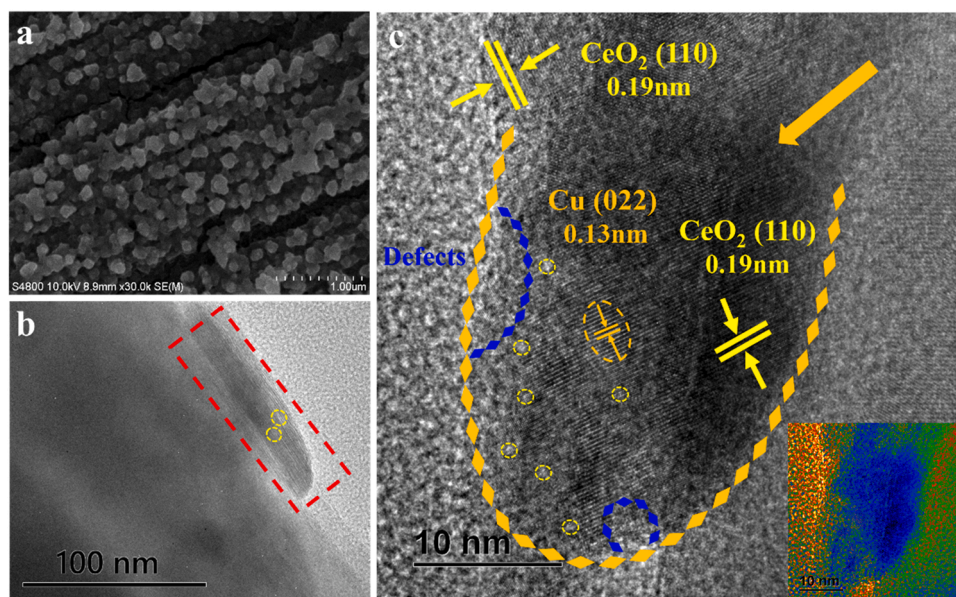


Fig. 7. Post-CO₂RR SEM (a), TEM (b) and HRTEM (c) images of the Cu/CeO₂-R catalyst.

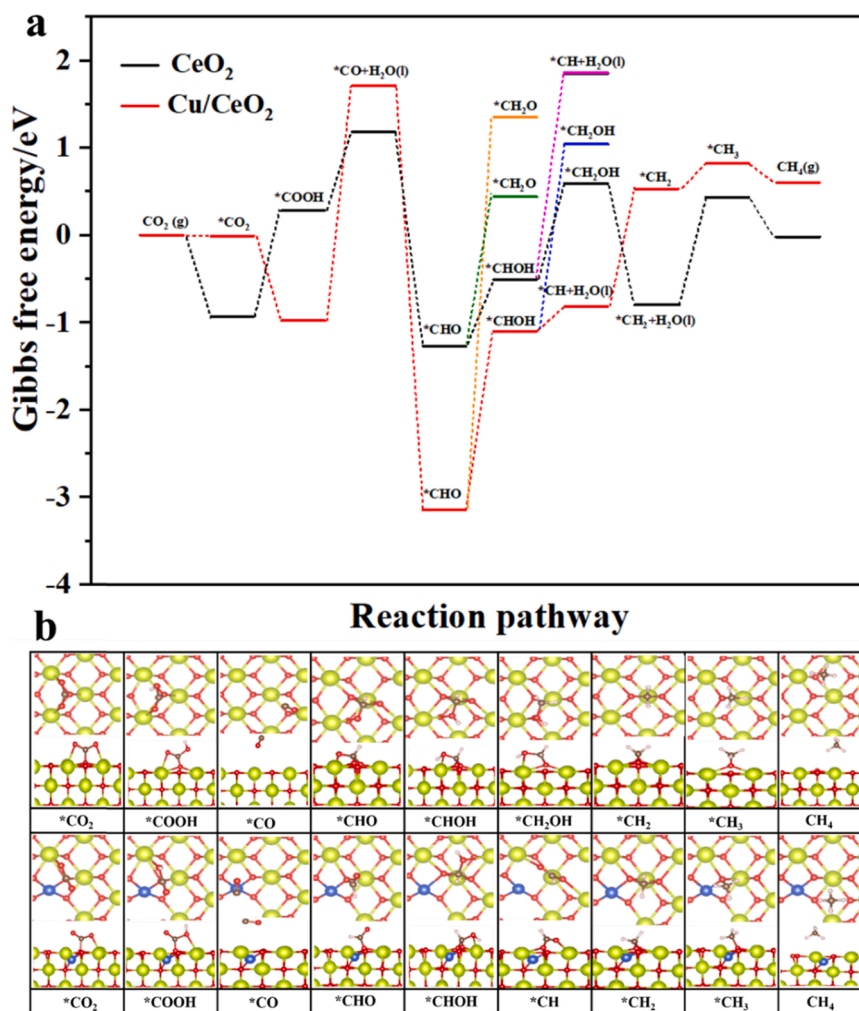


Fig. 8. (a) Free energy diagrams of the optimal reaction pathway, and (b) corresponding configurations on CeO₂ (above) and Cu/CeO₂ (below) catalysts. The Ce, Cu and O atoms are shown in green, blue and red, respectively.

*COOH intermediate to *CO through a non-spontaneous process on surface of CeO₂ and Cu/CeO₂ catalyst. Moreover, the transformation of *COOH to *CO is the limiting step with the highest reaction energy barrier on both CeO₂ and Cu/CeO₂, which would affect the catalytic activity of CO₂RR. Herein, as seen from Fig. S15, the *CO intermediate will be further hydrogenated to form *CHO rather than *COH or being desorbed from the catalyst surface as CO product. Subsequently, the hydrogenation of *CHO intermediate forms only *CHOH because of the much high increase in free energy of *CH₂O (1.71 eV for CeO₂ and 4.5 eV for Cu/CeO₂). In contrast, the *CHOH intermediate is further hydrogenated to *CH₂OH on pure CeO₂, while the formation of *CHOH to *CH on Cu/CeO₂ is more favorable due to its relatively lower free energy, implicating that the doping of Cu atoms on CeO₂ surface could change the reaction pathway of CO₂RR to some extent. Next, both *CH₂OH and *CH intermediates are converted to subsequent *CH₂ intermediate. Finally, CH₄ product is obtained through two hydrogenation steps of *CH₂. Overall, the optimal pathway for CH₄ product follows *CO₂ → *COOH → *CO → *CHO → *CHOH → *CH₂OH → *CH₂ → *CH₃ → CH₄ on CeO₂, while *CO₂ → *COOH → *CO → *CHO → *CHOH → *CH → *CH₂ → *CH₃ → CH₄ on Cu/CeO₂ catalyst. Obviously, the doping of Cu atom on CeO₂ surface lowers the reaction energy barrier of *CO₂ → *COOH and changes the reaction pathway from *CHOH → *CH₂OH to *CHOH → *CH, effectively improving the catalytic performance for CO₂RR. DFT calculations are also supported with the aforementioned experimental observations.

4. Discussion

In this joint experimental-computational work, the Cu/CeO₂ catalysts with different morphologies were synthesized for unraveling the conundrum of reaction mechanism in CO₂RR. Specifically, in stark contrast to the Cu/CeO₂-C and Cu/CeO₂-P, no recognizable diffraction peaks ascribed to Cu species appear in XRD patterns of the Cu/CeO₂-R and Cu/CeO₂-S catalysts, and their lattice parameters are smaller relative to those of their corresponding supports, implying that Cu species might be inserted into CeO₂ unit cell, in accordance with the UV-vis results. The nanorods are 8–15 nm in diameter and 200–300 nm in length with a growth direction along CeO₂ (110) facet, and the nanorod-like catalyst possesses the largest surface area, pore volume and ECSA in the four samples. The dislocation and lattice distortion are observed in HRTEM image, manifesting that the structural defects near the tips are formed for alleviating the tensile strain in the nanorod catalyst, and the XRD pattern and Raman spectrum confirm the existence of abundant defects in the Cu/CeO₂-R sample.

XPS analyses show that the Cu/CeO₂-R sample possesses the most surface divalent Cu species in line with the UV-vis results in addition to higher proportion of O-vacancy sites and adsorbed oxygen (O_{ad}) on oxygen deficiency regions. The surface Cu/Ce ratio of the Cu/CeO₂-R sample is same as the nominal one (Table 2), demonstrating that the rich porous architecture of the rod-shaped sample facilitates the dispersion of active Cu species within the catalyst, attractive for a favorable contact between the CO₂RR-relevant species and active sites. The results of band

gap energies indicate that the interaction between Cu and CeO₂ is the strongest on Cu/CeO₂-R, in favor of the generation of synergistic catalytic effect.

in situ DRIFTS manifests that CO₂ molecule chemisorbed on the surface CeO₂ acquires an electron to involve in the activation of CO₂, and the carbonyl species are rapidly protonated into *CHO at the nanointerfaces. The band intensities of CO₂, CO₂* and hydroxyls on the Cu/CeO₂-R are stronger than those on the Cu/CeO₂-S, demonstrating that the Cu/CeO₂-R has better capability of CO₂ adsorption and activation as well as H₂O dissociation, and consequently in favor of CO₂RR. DFT calculations proposed that the doping of Cu atom on CeO₂ surface lowers the reaction energy barrier of *CO₂ → *COOH and changes the reaction pathway from *CHOH → *CH₂OH to *CHOH → *CH, effectively improving the catalytic performance for CO₂RR. Quasi in situ ATR-FTIR corroborates the presence of relevant intermediates in the reaction pathway.

Intriguingly, the Cu/CeO₂ catalysts exhibit a clear CH₄ selectivity from CO₂RR in addition to C₂H₄, CO and H₂. The Cu/CeO₂-R catalyst exhibits the highest current density and TOF value for CH₄ production among the samples, and the current density reaches maximum together with a 49.3% Faradaic efficiency of CH₄ at −1.6 V. In the case of Cu/CeO₂-R, the lowest Tafel slope and the smallest charge transfer resistance correspond to its faster charge transfer from the catalyst surface to the adsorbed CO₂ molecule in the electrolyte to form *CO₂ intermediate that is medium-strength binding on this catalyst. Moreover, the Cu/CeO₂-R catalyst displays a relatively stable FE of CH₄ in 210 min. Post-CO₂RR SEM and TEM images evidence that the rod-shaped morphology is preserved in spite of the partial reduction of CeO₂ during electrocatalysis. As shown in Table S3, the Cu/CeO₂-R catalyst displays a comparable FE of CH₄ at −1.6 V.

5. Conclusions

To summarize, we synthesized the nanorod Cu/CeO₂ catalyst with abundant stepped and low-coordinated sites, stabilizing Cu species at the nanointerface. Taken together with Quasi in situ ATR-FTIR, in situ DRIFTS, *ex situ* characterizations and DFT theoretical simulations, the reaction pathway from CO₂ to CH₄ on Cu/CeO₂ catalyst is corroborated during CO₂RR for the first time. It is revealed that Cu species is inserted into CeO₂ unit cell in the Cu/CeO₂-R, and the XRD pattern and Raman spectrum confirm the existence of abundant defects. Its rich porous architecture facilitates the dispersion of active Cu species within the catalyst, attractive for a favorable contact between the CO₂RR-relevant species and active sites. The intimate interfacial interaction between Cu and CeO₂ is favorable for generation of synergistic catalytic effect. The Cu/CeO₂-R catalyst exhibits the highest current density and TOF value for CH₄ production among the samples, and the current density reaches maximum together with a 49.3% Faradaic efficiency of CH₄ at −1.6 V. DFT calculations reveal that the doping of Cu atom on CeO₂ surface lowers the reaction energy barrier of *CO₂ → *COOH and changes the reaction pathway from *CHOH → *CH₂OH to *CHOH → *CH, effectively improving the catalytic performance for CO₂RR. Quasi in situ ATR-FTIR and in situ DRIFTS validate the presence of related dynamic intermediates in the reaction pathway. The experimental and theoretical findings represent important progress toward understanding of the reaction mechanism of Cu/CeO₂ catalyst in electrocatalytic CO₂ reduction.

CRediT authorship contribution statement

Lei Xue: Conceptualization, Data curation, Formal analysis, Methodology, Resources, Software, Validation, Visualization, Writing-original draft, Writing-review & editing. **Chunjuan Zhang:** Performed the theoretical calculations. **Jinfang Wu:** Methodology, Validation, Writing-original draft, Writing-review & editing, Funding acquisition, Supervision. **Qi-Yuan Fan:** Theoretical calculations. **Yang Liu:** Formal analysis. **YanXin Wu:** Data curation, Software. **Jiaxin Li:** Investigation.

Heng Zhang: Methodology, Investigation. **Fenrong Liu:** Formal analysis, Performed the theoretical calculations. **Shanghong Zeng:** Conceptualization, Data curation, Formal analysis, Funding acquisition, Resources, Supervision.

Declaration of Competing Interest

The authors declare that they have no known competing financial interests or personal relationships that could have appeared to influence the work reported in this paper.

Acknowledgements

This work was supported financially by the National Natural Science Foundation of China (21968020, 22068026), the Natural Science Foundation of Inner Mongolia (grant 2018MS02020, 2018BS02008), and “Grassland Talent” Innovation Team of Inner Mongolia.

Appendix A. Supporting information

Supplementary data associated with this article can be found in the online version at doi:10.1016/j.apcatb.2021.120951.

References

- [1] C. Wang, X. Hu, X.S. Hu, X. Liu, Q.X. Guan, R. Hao, Y.P. Liu, W. Li, Typical transition metal single-atom catalysts with a metal-pyridine N structure for efficient CO₂ electroreduction, *Appl. Catal. B Environ.* 296 (2021), 120311.
- [2] T.N. Nguyen, M. Salehi, Q.V. Le, A. Seifitokaldani, C.T. Dinh, Fundamentals of electrochemical CO₂ reduction on single-metal-atom catalysts, *ACS Catal.* 10 (2020) 10068–10095.
- [3] T. Tsujiguchi, Y. Kawabe, S. Jeong, T. Ohto, S. Kukunuri, H. Kuramochi, Y. Takahashi, T. Nishiyuchi, H. Masuda, M. Wakasaka, K. Hu, G. Elumalai, J.-I. Fujita, Y. Ito, Acceleration of electrochemical CO₂ reduction to formate at the Sn/reduced graphene oxide interface, *ACS Catal.* 11 (2021) 3310–3318.
- [4] T.F. Liu, Q. Wang, G.X. Wang, X.H. Bao, Electrochemical CO₂ reduction on graphdiyne: a DFT study, *Green. Chem.* 23 (2021) 1212–1219.
- [5] X.Y. Ma, J.J. Du, H. Sun, F.H. Ye, X. Wang, P.F. Xu, C.G. Hu, L.P. Zhang, D. Liu, Boron, nitrogen co-doped carbon with abundant mesopores for efficient CO₂ electroreduction, *Appl. Catal. B Environ.* 298 (2021), 120543.
- [6] Y. Huang, X.N. Mao, G.T. Yuan, D. Zhang, B.B. Pan, J. Deng, Y.R. Shi, N. Han, C. R. Li, L. Zhang, L. Wang, L. He, Y.Y. Li, Y.G. Li, Size-dependent selectivity of electrochemical CO₂ reduction on converted In₂O₃ nanocrystals, *Angew. Chem. Int. Ed.* 60 (2021) 15844–15848.
- [7] K. Ye, T.F. Liu, Y.P. Song, Q. Wang, G.X. Wang, Tailoring the interactions of heterogeneous Ag₂S/Ag interface for efficient CO₂ electroreduction, *Appl. Catal. B Environ.* 296 (2021), 120342.
- [8] J.G. Wang, S.L. Ning, M. Luo, D. Xiang, W. Chen, X.W. Kang, Z. Jiang, S.W. Chen, In-Sn alloy core-shell nanoparticles: In-doped SnOx shell enables high stability and activity towards selective formate production from electrochemical reduction of CO₂, *Appl. Catal. B Environ.* 288 (2021), 119979.
- [9] Q. Zhao, J.M.P. Martinez, E.A. Carter, Revisiting understanding of electrochemical CO₂ reduction on Cu (111): Competing proton-coupled electron transfer reaction mechanisms revealed by embedded correlated wavefunction theory, *J. Am. Chem. Soc.* 143 (2021) 6152–6164.
- [10] D. Li, L.L. Huang, Y. Tian, T. Liu, L. Zhen, Y. Feng, Facile synthesis of porous Cu-Sn alloy electrode with prior selectivity of formate in a wide potential range for CO₂ electrochemical reduction, *Appl. Catal. B Environ.* 292 (2021), 120119.
- [11] J.C. Wang, T. Cheng, A.Q. Fenwick, T.N. Baroud, A. Rosas-Hernandez, J.H. Ko, Q. Gan, W.A. Goddard, R.H. Iii, Grubbs, Selective CO₂ electrochemical reduction enabled by a tricomponent copolymer modifier on a copper surface, *J. Am. Chem. Soc.* 143 (2021) 2857–2865.
- [12] S. Jin, Z.M. Hao, K. Zhang, Z.H. Yan, J. Chen, Advances and challenges for the electrochemical reduction of CO₂ to CO: From fundamentals to industrialization, *Angew. Chem. Int. Ed.* 60 (2021) 2–24.
- [13] L. Zhang, X.-X. Li, Z.L. Lang, Y. Liu, J. Liu, L. Yuan, W.-Y. Lu, Y.-S. Xia, L.-Z. Dong, D.-Q. Yuan, Y.-Q. Lan, Enhanced cuprophilic interactions in crystalline catalysts facilitate the highly selective electroreduction of CO₂ to CH₄, *J. Am. Chem. Soc.* 143 (2021) 3808–3816.
- [14] C.-J. Chang, S.-C. Lin, H.-C. Chen, J.L. Wang, K.J. Zheng, Y.P. Zhu, H.M. Chen, Dynamic reoxidation/reduction-driven atomic interdiffusion for highly selective CO₂ reduction toward methane, *J. Am. Chem. Soc.* 142 (2020) 12119–12132.
- [15] J.L. Wang, H.-Y. Tan, Y.P. Zhu, H. Chu, H.M. Chen, Linking the dynamic chemical state of catalysts with the product profile of electrocatalytic CO₂ reduction, *Angew. Chem. Int. Ed.* 60 (2021) 17254–17267.
- [16] L.L. Han, S.J. Song, M.J. Liu, S.Y. Yao, Z.X. Liang, H. Cheng, Z.H. Ren, W. Liu, R. Q. Lin, G.C. Qi, X.J. Liu, Q. Wu, J. Luo, H.L.L. Xin, Stable and efficient single-atom Zn catalyst for CO₂ reduction to CH₄, *J. Am. Chem. Soc.* 142 (2020) 12563–12567.

- [17] A.R. Haines, J.C. Hemminger, Stability of Cu/TiO₂ nanoparticle model catalysts under electrochemical CO₂ reduction conditions, *ACS Catal.* 11 (2021) 6960–6970.
- [18] X.-Q. Li, G.-Y. Duan, J.-W. Chen, L.-J. Han, S.-J. Zhang, B.-H. Xu, Regulating electrochemical CO₂RR selectivity at industrial current densities by structuring copper@poly(ionic liquid) interface, *Appl. Catal. B Environ.* 297 (2021), 120471.
- [19] Y.J. Yang, J. Liu, D.W. Wu, J.Y. Ding, B. Xiong, Two-dimensional pyrite supported transition metal for highly-efficient electrochemical CO₂ reduction: A theoretical screening study, *Chem. Eng. J.* 424 (2021), 130541.
- [20] S.Z. Zhao, D.J. Kang, Y.P. Liu, Y.F. Wen, X.Z. Xie, H.H. Yi, X.L. Tang, Spontaneous formation of asymmetric oxygen vacancies in transition-metal-Doped CeO₂ nanorods with improved activity for carbonyl sulfide hydrolysis, *ACS Catal.* 10 (2020) 11739–11750.
- [21] X. Liu, S.F. Jia, M. Yang, Y.T. Tang, Y.W. Wen, S.Q. Chu, J.B. Wang, B. Shan, R. Chen, Activation of subnanometric Pt on Cu-modified CeO₂ via redox-coupled atomic layer deposition for CO oxidation, *Nat. Commun.* 11 (2020) 4240.
- [22] J.D. Zhu, Y.Q. Su, J.C. Chai, V. Muravev, N. Kosinov, E.J.M. Hensen, Mechanism and nature of active sites for methanol synthesis from CO/CO₂ on Cu/CeO₂, *ACS Catal.* 10 (2020) 11532–11544.
- [23] A. Davó-Quinónero, E. Bailón-García, S. López-Rodríguez, J. Juan-Juan, D. Lozano-Castelló, M. García-Melchor, F.C. Herrera, E. Pellegrin, C. Escudero, A. Bueno-López, Insights into the oxygen vacancy filling mechanism in CuO/CeO₂ catalysts: A key step toward high selectivity in preferential CO oxidation, *ACS Catal.* 10 (2020) 6532–6545.
- [24] K. Chang, H.C. Zhang, M.-J. Cheng, Q. Lu, Application of ceria in CO₂ conversion catalysis, *ACS Catal.* 10 (2019) 613–631.
- [25] B.B. Wang, H. Zhang, W. Xu, X.B. Li, W. Wang, L.J. Zhang, Y.M. Li, Z. Peng, F. Yang, Z. Liu, Nature of active sites on Cu–CeO₂ catalysts activated by high-temperature thermal aging, *ACS Catal.* 10 (2020) 12385–12392.
- [26] D.F. Gao, Y. Zhang, Z.W. Zhou, F. Cai, X.F. Zhao, W.G. Huang, Y.S. Li, J.F. Zhu, P. Liu, F. Yang, G.X. Wang, X.H. Bao, Enhancing CO₂ electroreduction with the metal-oxide interface, *J. Am. Chem. Soc.* 139 (2017) 5652–5655.
- [27] M. Lykaki, E. Pachatouridou, S.A.C. Carabineiro, E. Iliopoulou, C. Andriopoulou, N. Kallithrakas-Kontose, S. Boghosian, M. Konsolakis, Ceria nanoparticles shape effects on the structural defects and surface chemistry: Implications in CO oxidation by Cu/CeO₂ catalysts, *Appl. Catal. B Environ.* 230 (2018) 18–25.
- [28] J.H. Li, Z.Q. Liu, D.A. Cullen, W.H. Hu, J. Huang, L.B. Yao, Z.M. Peng, P.L. Liao, R. G. Wang, Distribution and valence state of Ru species on CeO₂ supports: support shape effect and its influence on CO oxidation, *ACS Catal.* 9 (2019) 11088–11103.
- [29] S.B. Varandili, J. Huang, E. Oveis, G.L. De Gregorio, M. Mensi, M. Strach, J. Vavra, C. Gadiyar, A. Bhowmik, R. Buonsanti, Synthesis of Cu/CeO₂-x nanocrystalline heterodimers with interfacial active sites to promote CO₂ electroreduction, *ACS Catal.* 9 (2019) 5035–5046.
- [30] F. Jiang, S.S. Wang, B. Liu, J. Liu, L. Wang, Y. Xiao, Y.B. Xu, X.H. Liu, Insights into the influence of CeO₂ crystal facet on CO₂ hydrogenation to methanol over Pd/CeO₂ catalysts, *ACS Catal.* 10 (2020) 11493–11509.
- [31] A. Trovarelli, J. Llorca, Ceria catalysts at nanoscale: How do crystal shapes shape catalysis? *ACS Catal.* 7 (2017) 4716–4735.
- [32] Z.D. Huang, L. Shang, H.Y. Qi, Z. Zhao, B.F. Tu, W.S. Yang, M.J. Cheng, Charge transfer reactions in CO₂ electroreduction on manganese doped ceria, *ChemElectroChem* 10.1002/celc.201801427.
- [33] Y.F. Wang, Z. Chen, P. Han, Y.H. Du, Z.X. Gu, X. Xu, G.F. Zheng, Single-atomic Cu with multiple oxygen vacancies on ceria for electrocatalytic CO₂ reduction to CH₄, *ACS Catal.* 8 (2018) 7113–7119.
- [34] S.L. Chu, X.P. Yan, C. Choi, S. Hong, A.W. Robertson, J. Masa, B.X. Han, Y.J. Jung, Z.Y. Sun, Stabilization of Cu⁺ by Tuning a CuO–CeO₂ interface for selective electrochemical CO₂ reduction to ethylene, *Green. Chem.* 22 (2020) 6540–6546.
- [35] F. Wang, W. Li, X. Feng, D.P. Liu, Y. Zhang, Decoration of Pt on Cu/Co double-doped CeO₂ nanospheres and their greatly enhanced catalytic activity, *Chem. Sci.* 7 (2016) 1867–1873.
- [36] Y.S. Xi, Y. Wang, D.W. Yao, A.T. Li, J.Y. Zhang, Y.J. Zhao, J. Lv, X.B. Ma, Impact of the oxygen vacancies on copper electronic state and activity of Cu-based catalysts in the hydrogenation of methyl acetate to ethanol, *ChemCatChem* 11 (2019) 2607–2614.
- [37] D.J. Kang, X.L. Yu, M.F. Ge, Morphology-dependent properties and adsorption performance of CeO₂ for fluoride removal, *Chem. Eng. J.* 330 (2017) 36–43.
- [38] M. Lykaki, E. Pachatouridou, S.A.C. Carabineiro, E. Iliopoulou, C. Andriopoulou, N. Kontos, S. Boghosian, M. Konsolakis, Ceria nanoparticles shape effects on the structural defects and surface chemistry: Implications in CO oxidation by Cu/CeO₂ catalysts, *Appl. Catal. B Environ.* 230 (2018) 18–28.
- [39] Z.X. Zhang, Y.H. Wang, J.M. Lu, J. Zhang, M.R. Li, X.B. Liu, F. Wang, Pr-doped CeO₂ catalyst in the prins condensation-hydrolysis reaction: Are all of the defect sites catalytically active? *ACS Catal.* 8 (2018) 2635–2644.
- [40] Z.C. Tan, G.C. Li, H.-L. Chou, Y.Y. Li, X.F. Yi, A.H. Mahadi, A. Zheng, S.C. Edman Tsang, Y.-K. Peng, Differentiating surface Ce species among CeO₂ facets by solid-state NMR for catalytic correlation, *ACS Catal.* 10 (2020) 4003–4011.
- [41] Y.P. Zhu, T.-R. Kuo, Y.-H. Li, M.-Y. Qi, G. Chen, J.L. Wang, Y.-J. Xu, H.M. Chen, Emerging dynamic structure of electrocatalyst unveiled by in situ X-ray diffraction/absorption spectroscopy, *Energy Environ. Sci.* 14 (2021) 1928–1958.
- [42] G.W. Woyessa, J.-a B. dela Cruz, M. Rameez, C.-H. Hung, Nanocomposite catalyst of graphitic carbon nitride and Cu/Fe mixed metal oxide for electrochemical CO₂ reduction to CO, *Appl. Catal. B Environ.* 291 (2021), 120052.
- [43] Q.Y. Wang, Y.X. Li, A. Serrano-Lotina, W. Han, R. Portela, R. Wang, M.A. Banares, K.L. Yeung, Operando Investigation of toluene oxidation over 1D Pt@CeO₂ derived from Pt cluster-containing MOF, *J. Am. Chem. Soc.* 143 (2021) 196–205.
- [44] M. Guo, J. Lu, Y. Wu, Y. Wang, M. Luo, UV and visible raman studies of oxygen vacancies in rare-earth-doped ceria, *Langmuir* 27 (2011) 3872–3877.
- [45] H. Deol, S. Pramanik, M. Kumar, I.A. Khan, V. Bhalla, Supramolecular ensemble of a TICT-AIEE active pyrazine derivative and CuO NPs: A potential photocatalytic system for sonogashira couplings, *ACS Catal.* 6 (2016) 3771–3783.
- [46] Z.X. Gu, N. Yang, P. Han, M. Kuang, B.B. Mei, Z. Jiang, J. Zhong, L. Li, G.F. Zheng, Oxygen vacancy tuning toward efficient electrocatalytic CO₂ reduction to C₂H₄, *Small Methods* (2018) 1800449.
- [47] Y. Xie, J.F. Wu, G.J. Jing, H. Zhang, S.H. Zeng, X.P. Tian, X.Y. Zou, J. Wen, H.Q. Su, C.-J. Zhong, P.X. Cui, Structural origin of high catalytic activity for preferential CO oxidation over CuO/CeO₂ nanocatalysts with different shapes, *Appl. Catal. B Environ.* 239 (2018) 665–676.
- [48] X.D. Li, Y.F. Sun, J.Q. Xu, Y.J. Shao, J. Wu, X.L. Xu, Y. Pan, H.X. Ju, J.F. Zhu, Y. Xie, Selective visible-light-driven photocatalytic CO₂ reduction to CH₄ mediated by atomically thin CuIn₅S₈ layers, *Nat. Energy* 4 (2019) 690–699.
- [49] S.Q. Zhu, T.H. Li, W.-B. Cai, M.H. Shao, CO₂ Electrochemical reduction As probed through infrared spectroscopy, *ACS Energy Lett.* 4 (2019) 682–689.
- [50] M. Moradzaman, G. Mul, Infrared analysis of interfacial phenomena during electrochemical reduction of CO₂ over polycrystalline copper electrodes, *ACS Catal.* 10 (2020) 8049–8057.
- [51] M. Wang, M. Shen, X.X. Jin, J.J. Tian, Y.J. Zhou, Y.R. Shao, L.X. Zhang, Y.S. Li, J. L. Shi, Mild generation of surface oxygen vacancies on CeO₂ for improved CO₂ photoreduction activity, *Nanoscale* 12 (2020) 12374–12382.
- [52] W.-W. Wang, W.-Z. Yu, P.-P. Du, H. Xu, Z. Jin, R. Si, C. Ma, S. Shi, C.-J. Jia, C.-H. Yan, Crystal plane effect of ceria on supported copper oxide cluster catalyst for CO oxidation: Importance of metal-support interaction, *ACS Catal.* 7 (2017) 1313–1329.
- [53] S.Y. Yao, K. Mudiyansele, W.Q. Xu, A.C. Johnston-Peck, J.C. Hanson, T. Wu, D. Stacchiola, J.A. Rodriguez, H. Zhao, K.A. Beyer, K.W. Chapman, P.J. Chupas, A. Martínez-Arias, R. Si, T.B. Bolin, W. Liu, S.D. Senanayake, Unraveling the dynamic nature of a CuO/CeO₂ catalyst for CO oxidation in operando: A combined study of XANES (Fluorescence) and DRIFTS, *ACS Catal.* 4 (2014) 1650–1661.
- [54] B. Liu, C.M. Li, G.Q. Zhang, X.S. Yao, S.S.C. Chuang, Z. Li, Oxygen vacancy promoting dimethyl carbonate synthesis from CO₂ and methanol over Zr-doped CeO₂ nanorods, *ACS Catal.* 8 (2018) 10446–10456.
- [55] M.C. Luo, Z.Y. Wang, Y.G.C. Li, J. Li, F.W. Li, Y. Lum, D.H. Nam, B. Chen, J. Wicks, A. Xu, T. Zhuang, W.R. Leow, X. Wang, C.T. Dinh, Y. Wang, Y. Wang, D. Sinton, E. H. Sargent, Hydroxide promotes carbon dioxide electroreduction to ethanol on copper via tuning of adsorbed hydrogen, *Nat. Commun.* 10 (2019) 5814.
- [56] Z.D. Li, D. He, X.X. Yan, S. Dai, S. Younan, Z.J. Ke, X.Q. Pan, X.H. Xiao, H.J. Wu, J. Gu, Size-dependent nickel-based electrocatalysts for selective CO₂ reduction, *Angew. Chem. Int. Ed.* 59 (2020) 18572–18577.
- [57] W. Zhang, C.H. Huang, Q. Xiao, L. Yu, L. Shuai, P. An, J. Zhang, M. Qiu, Z. Ren, Y. Yu, Atypical oxygen-bearing copper boosts ethylene selectivity toward electrocatalytic CO₂ reduction, *J. Am. Chem. Soc.* 142 (2020) 11417–11427.
- [58] S.-C. Lin, C.-C. Chang, S.-Y. Chiu, H.-T. Pai, T.-Y. Liao, C.-S. Hsu, W.-H. Chiang, M.-K. Tsai, H.M. Chen, Operando time-resolved X-ray absorption spectroscopy reveals the chemical nature enabling highly selective CO₂ reduction, *Nat. Commun.* 11 (2020) 3525.
- [59] A. Sasahara, C.L. Pang, H. Onishi, Probe microscope observation of platinum atoms deposited on the TiO₂(110)-(1 × 1) surface, *J. Phys. Chem. B* 110 (2006) 13453–13457.
- [60] Z. Novotný, G. Argentero, Z.M. Wang, M. Schmid, U. Diebold, G.S. Parkinson, Ordered array of single adatoms with remarkable thermal stability: Au/Fe₃O₄(001), *PRL* 108 (2012), 216103.
- [61] C.-J. Chang, S.-F. Hung, C.-S. Hsu, H.-C. Chen, S.-C. Lin, Y.-F. Liao, H.M. Chen, Quantitatively unraveling the redox shuttle of spontaneous oxidation/electroreduction of CuOx on silver nanowires using in situ X-ray absorption spectroscopy, *ACS Cent. Sci.* 5 (2019) 1998–2009.